Applied Surface Science 580 (2022) 152267

Contents lists available at ScienceDirect

Applied Surface Science

journal homepage: www.elsevier.com/locate/apsusc

Full Length Article

Role of the metal supply pathway on silicon patterning by oblique ion beam sputtering

A. Redondo-Cubero [a,b], F.J. Palomares [c], K. Lorenz [d,e], J. Rubio-Zuazo [c,f], R. Hübner [g], F. J. Mompeán [c], M. García-Hernández [c], G.R. Castro [c,f], L. Vázquez [c,*]

[a] Grupo de Electrónica y Semiconductores, Departamento de Física Aplicada, Universidad Autónoma de Madrid, 28049 Madrid, Spain
[b] Centro de Micro-Análisis de Materiales, Universidad Autónoma de Madrid, C/ Faraday 2, 28049 Madrid, Spain
[c] Instituto de Ciencia de Materiales de Madrid, Consejo Superior de Investigaciones Científicas, 28049 Madrid, Spain
[d] Instituto Superior Técnico, Universidade de Lisboa, Estrada Nacional 10, km 139.7, 2695-066 Bobadela LRS, Portugal
[e] Instituto de Engenharia de Sistemas e Computadores - Microsistemas e Nanotecnologia (INESC- MN), Rua Alves Redol 9, 1000-029 Lisboa, Portugal
[f] SpLine Spanish CRG Beamline at the ESRF, ESRF-BP 220-38043 Grenoble, Cedex, France
[g] Institute of Ion Beam Physics and Materials Research, Helmholtz-Zentrum Dresden-Rossendorf, D-01328 Dresden, Germany

ARTICLE INFO

Keywords:
Surface nanopatterning
Ion beam sputtering
Silicon
Magnetic properties
Silicides
Iron

ABSTRACT

The dynamics of the pattern induced on a silicon surface by oblique incidence of a 40 keV Fe ion beam is studied. The results are compared with those obtained for two reference systems, namely a noble gas ion beam either without or with Fe co-deposition. The techniques employed include Atomic Force Microscopy, Rutherford Backscattering Spectrometry, Transmission Electron Microscopy, X-ray Photoelectron and hard X-ray photoelectron spectroscopies, as well as Superconducting Quantum Interference Device measurements. The Fe-induced pattern differs from those of both reference systems since a pattern displaying short hexagonal ordering develops, although it shares some features with them. In both Fe systems a chemical pattern, with iron silicide-rich and -poor regions, is formed upon prolonged irradiation. The metal pathway has a marked influence on the patterns' morphological properties and on the spatial correlation between the chemical and morphological patterns. It also determines the iron silicide stoichiometry and the surface pattern magnetic properties that are better for the Fe-implanted system. These results show that in ion-beam-induced silicon surface patterning with reactive metals, the metal supply pathway is critical to determine not only the morphological pattern properties, but also the chemical and magnetic ones.

1. Introduction

Ion beam sputtering (IBS) has become an efficient and affordable technique to induce different nanopatterns on relatively large surface areas of a variety of materials, including semiconductors, metals and dielectrics [1-3]. Most of the efforts in the last years have been focused on studying IBS patterning of a silicon surface due to its extreme flatness and technological relevance [4]. When a silicon target is irradiated by a noble gas ion beam, a nano-rippled pattern is induced on the surface provided the ion beam incidence angle, θ, is larger than a threshold angle, θ_{th}, which is about 45°–50°. This is understood from the interplay between the sputtering yield dependence on the surface curvature, known as the Bradley-Harper (BH) effect [5], and the so-called Carter-Vishnyakov (CV) effect [6]. The former effect causes a surface instability as the surface troughs present a higher sputtering yield than the crests. The latter is due to the surface atomic currents caused by the impinging ions [7,8]. This effect is morphologically stabilizing for ion incident angles below $\sim 45°$ but becomes destabilizing for larger angles [9]. Thus, for $\theta < 50°$, the silicon surface remains flat upon ion irradiation because of the predominance of the stabilizing CV effect, while for larger angles, a clear ripple pattern develops.

This scenario changes drastically when a metal flux lands on the target surface simultaneously with the ion beam irradiation. This is usually achieved by placing a metal plate adjacent to or surrounding the silicon surface whose sputtered atoms land on the irradiated silicon target [10-14]. Under these conditions, ripple or dot patterns are produced on the surface for angles $\theta < \theta_{th}$ and even for normal-incidence ion irradiation. In these cases, the metal flux orientation with respect to that

* Corresponding author.
E-mail address: lvb@icmm.csic.es (L. Vázquez).

https://doi.org/10.1016/j.apsusc.2021.152267
Received 20 October 2021; Received in revised form 2 December 2021; Accepted 16 December 2021
Available online 20 December 2021

of the ion beam plays an important role to define the pattern properties [12]. The experimental results evidence the existence of a coupling between composition and surface morphologies, which reveals that the metal supply is a key parameter for IBS patterning. Furthermore, different studies have addressed the role played by the capacity of the metal atom to chemically react with the silicon atoms to form silicides. On the one hand, several studies confirm that patterns develop when the metal forms a silicide that shows a lower sputtering yield than silicon [15,16]. The low sputtering yield regions lead to surface instabilities as they protrude with respect to the silicon ones. On the other hand, other reports show that patterns are also produced when the metal, such as gold, does not form a silicide [17,18].

In general, the metal supply opens the possibility of producing a larger variety of nanopattern morphologies [19] as well as to achieve highly ordered ones [20,21]. Because of this appealing potential, this sort of IBS patterning has motivated both the theoretical modelling [22,23] and the experimental work [10-14] for normal or near-normal ion incidence conditions, where the induced patterns are indeed due to the key role played by the metal flux. In contrast, scarce experimental and theoretical studies have been performed for IBS patterning with metal co-deposition for $\theta > \theta_{th}$, i.e. for conditions at which ripple patterns are also produced in the absence of a metal flux, and where other destabilizing effects, beyond the BH and CV ones, come into play, such as implantation [24]. Here, two scenarios can be considered: (i) the standard one where a noble gas ion beam impacts at $\theta > \theta_{th}$ with simultaneous metal co-deposition coming from the opposite direction [25,26]; (ii) that one where the ion species is metallic and impinges on the target surface at $\theta > \theta_{th}$. In the latter case, two main systems have been addressed. In the first one, an Au^+ ion beam bombarded Ge or Si surfaces [27-29], whereas in the second one, Fe^+ ions impacted on a Si surface [30-32]. It is important to note that Au and Si (Ge) do not form a compound, whereas iron and silicon do form a silicide with consequences on the local sputtering yield.

In the present experiments, Fe has been chosen as the foreign species because is one of the most widely used in this sort of patterning [11-16,21,22,25,30-32]. In addition, due to its magnetic and conductive character, its use in IBS patterning experiments may lead also to self-organized conducting and magnetic nanostructures. It should be noted that the achievement of ordered patterns of magnetic structures may find applications in electronic, magnetic and sensing devices [32-38].

In this work, we aim at analyzing how the Fe supply pathway affects the pattern characteristics when ion irradiation takes place for $\theta > \theta_{th}$. In the main case of the study, the ions themselves are metallic whereas in the other one the metal supply comes from an adjacent plate, i.e. from the opposite direction to that of a noble gas ion beam. We compare their morphological pattern dynamics, as well as the nature of the corresponding compositional patterns, plus that one of a reference system. Specifically, we study the pattern dynamics of Si(100) directly irradiated with either a 40 keV Fe^+ ion beam (Fe system), a 40 keV Ar^+ ion beam with directional Fe co-deposition (Ar + Fe system), and 40 keV Xe^+ ions (Xe, reference, system). In all cases, $\theta = 60^\circ$ and the fluence was the only variable parameter. Medium ion energy was chosen because previous studies showed that the morphologically and compositionally induced effects are more marked and easy to measure by various techniques [14,21,25]. In this sense, the samples of this study were extensively analyzed by different morphological and compositional techniques.

2. Experimental

2.1. Sample preparation

The irradiation experiments were performed in a Danfysik 1090 ion implanter with a base pressure of $5{\cdot}10^{-6}$ mbar. The ions impinged on single crystalline Si(1 0 0) targets (12 × 12 mm^2) at $\theta = 60^\circ \pm 5^\circ$ with respect to the surface normal with a current density of 18 μA cm^{-2} in the sample plane. Three sets of samples were prepared using different ion species: 40 keV Xe^+ (reference of non-metallic implantation), 40 keV Fe^+ (pure metal implantation), and 40 keV Ar^+ (with metal co-deposition).

The Xe system was used as a control, since it represents the pattern formation in the absence of impurities. To avoid any unwanted metal supply from the surrounding sample holder plate, the sample was placed on top of a 10-mm-high cylinder with 10-mm diameter. The fluence was varied from 10^{16} up to $4{\cdot}10^{18}$ cm^{-2}. The average projected range of Xe ions into Si according to SRIM simulations [39] is 14.3 nm with a straggling of 6.5 nm, i.e., the maximum projected range (3σ) is ~ 42 nm. The estimated by SRIM Si sputtering yield is 9.04 atoms/ion. It is important to note that, although the natural choice for these reference samples would be Ar, we have selected Xe because the dynamics is much faster due to its heavier mass, which allows us to analyze the dynamics over a wider temporal range.

The Fe system is the main interest in this work. The fluence was varied from 10^{16} up to $4{\cdot}10^{18}$ cm^{-2}. The average projected range of Fe ions into Si according to SRIM simulations is 20.7 nm with a straggling of 12.0 nm, i.e., the maximum projected range is ~ 65 nm. The estimated sputtering yield of Fe is 5.91 atoms/ion, which is very similar to that of the Si target (5.89 atoms/ion).

Finally, in the Ar + Fe system, a steel plate (1.5 mm height) was placed adjacent to the Si target. To achieve homogeneous irradiation, the focused beam was scanned with a magnetic x-y sweeping system. The irradiation times spanned from 20 min to 16 h, implying fluences from $2{\cdot}10^{17}$ up to $6.5{\cdot}10^{18}$ cm^{-2}. In this set-up, the metal supply is quite directional and opposite to that of the ion beam. The average projected range of Ar ions into Si according to SRIM simulations is 26.1 nm with a straggling of 15.0 nm, i.e., the total projected range is ~ 90 nm. The estimated Si sputtering yield is 4.18 atoms/ion. However, in this case, the sputtering yield for the Fe atoms in the metal plate is also relevant, since this yield controls the pace of the metal supply on the Si surface. SRIM simulations estimate the sputtering yield of Fe (note that the local incidence angle for the metal plate is not 60° but 30°) to be 5.62 atoms/ion. It should be noted that this system was extensively studied previously by some of the present authors [25]. Therefore, here, we will use these data for comparison and interpretation purposes.

2.2. Microscopic characterization

The surface morphology was characterized ex-situ by atomic force microscopy (AFM) with two systems namely, a Nanoscope IIIa (Veeco) and a PicoPlus 5500 (Agilent) operating in intermittent contact mode with silicon cantilevers with a nominal radius of curvature, r, of 8 nm and an opening angle, φ, smaller than 52° (Bruker). From these data, and using the Gwyddion freeware package [40], the global surface roughness of each sample was obtained as well as other statistical functions.

In particular, extensive use of the Power Spectral Density (PSD) function has been made in order to obtain the corresponding wavelength value, λ, of the ripple patterns. This is straightforward to do when the pattern is clear and the PSD does display a clear peak at $k_0 = 1/\lambda$ [41]. As most of the patterns have the wave vector parallel to the projected ion beam, we have usually performed this analysis by using $PSD_{||}$, i.e. the PSD along this direction. In contrast, when the surface presents a facetted or more disordered pattern, the corresponding $PSD_{||}$, in a logarithmic plot, does not show any clear peak but a linear region with a negative slope for high k values and a horizontal, saturated, region at low k values [42]. In this case, k_0 lies at the crossover point between these two regions. From the slope, m, of the negatively sloped regions, the corresponding value of the so-called roughness exponent, α, can be derived based on the relationship: $m = -(2\alpha + 1)$ [42].

Current sensing AFM (CS-AFM) measurements were performed with the Agilent microscope. Several cantilevers were employed: Pt-coated (OMCL-AC240TM, r < 25 nm and φ < 70°, from Olympus), DPER18 (r ~ 15 nm and φ < 32°, from MikroMasch), diamond-coated CDT-FMR

(r ~ 83 nm and φ < 47°, from NanoWorld), and DCP11 (r ~ 60 nm and φ < 44°, from NT-MDT). The sample bias applied was in the 5–8 V range. The CS-AFM measurements were performed under nitrogen ambient to avoid current contributions from water vapor adsorbed on the surface. Magnetic force microscopy (MFM) imaging was performed using MESP cantilevers (Bruker) with a nominal radius of 35 nm.

Transmission electron microscopy (TEM) analysis in cross-sectional geometry was performed using an image-C_s-corrected Titan 80–300 microscope (FEI) operated at an accelerating voltage of 300 kV. Besides bright-field TEM imaging, element mapping using energy-filtered TEM based on the three-window-method at the Si-$L_{2,3}$, O-K, Fe-$L_{2,3}$, or Xe-$M_{4,5}$ edges was done employing a Gatan Imaging Filter 863. Prior to TEM analysis, the specimen mounted in a double-tilt low-background holder was placed for 10 s into a Model 1020 Plasma Cleaner (Fischione) to remove possible contamination. Classical TEM cross-sections of the samples glued together in face-to-face geometry using G2 epoxy glue (Gatan) were prepared by sawing (Wire Saw WS 22, IBS GmbH), grinding (MetaServ 250, Bühler), polishing (Minimet 1000, Bühler), dimpling (Dimple Grinder 656, Gatan), and final Ar ion milling (Precision Ion Polishing System PIPS 691, Gatan).

2.3. Compositional analysis

The composition of the irradiated surfaces was determined by means of Rutherford backscattering spectrometry (RBS) [43]. A 2 MeV He^+ beam (1 mm^2 size) was used, and the backscattered particles were detected with a Si solid state detector at a scattering angle of 170º (energy resolution of 16 keV). A 3-axis goniometer was employed to control the crystal position with an accuracy of 0.01°. RBS spectra in channeling (RBS/C) and random geometry were acquired to characterize the ion-induced amorphous layer.

The surface composition was also evaluated by X-ray photoelectron spectroscopy (XPS) and hard X-ray photoelectron spectroscopy (HAXPES). In the first case, a SPECS Phoibos 150 spectrometer with a hemispherical analyzer using monochromatic Al Kα radiation was employed. Fe 2p and Si 2p core-level XPS spectra were recorded using an energy step of 0.05 eV and a pass energy of 10 eV, which provides an overall energy resolution of ~ 0.40 eV. The spectra were acquired at take-off angles from normal (90°) to grazing (15°) emission in order to study correlations between surface morphology and composition. Note that, under grazing emission, the signal from the outermost surface region is also enhanced. Data analysis was performed using the Casa XPS processing software (Casa Software Ltd., Cheshire, UK). The integral peak areas after background subtraction and normalization using sensitivity factors were taken to calculate the atomic concentration of each element.

The HAXPES experiments were done at the Spanish CRG SpLine beamline (BM25) of the ESRF synchrotron (Grenoble, France) [44]. HAXPES is a non-destructive compositional analysis technique that allows depth profiling in the tens-of-nanometer scale thanks to the capability of tuning the X-ray excitation energy [45]. In our study, three different photon energies (9.0, 10.5, and 14.0 keV) were used, recording spectra for several energy levels: Fe 1s (7112.0 eV), Fe 2p1/2 (721.1 eV), Fe 2p3/2 (708.1 eV), Fe 3s (92.9 eV), Si 1s (1839.0 eV), and O 1s (543.1 eV). The photon incident angle was set to 2° with respect to the sample surface and the electron emission angle was fixed to 15° on the forward direction, from the normal to the sample surface. The overall energy resolution lies, depending on the photon energy and pass energy, within a range from 1.6 to 2.8 eV.

2.4. Magnetic characterization

The magnetic characterization of the samples was carried out using a superconducting quantum interference device (SQUID) from Quantum Design equipped with a 5 Tesla coil. The thermal dependence of the magnetization was measured after a zero field cooling (ZFC) and after a 5 Tesla field cooling (FC), being 5 10^{-3} Tesla the measuring field in both cases. Isotherm hysteresis cycles were measured at 4 K.

3. Results

3.1. Evolution of the pattern morphology

First, it is worth to comment on the uniformity of the surface patterning for each system. Thus, for those where either Xe^+ or Fe^+ ions were employed, practically the whole target area (around 12 × 12 mm^2) was homogenously patterned. In contrast, for the Ar + Fe system, as it was described elsewhere [25], the pattern does depend on the distance from the steel plate. Thus, for this system we present the data corresponding to a distance to the plate of 3 mm (see [25] for more details). The AFM images taken for the two reference/control systems, for increasing fluences, are shown in Fig. 1a, b. In both cases, the surface remains featureless until attaining a fluence of 10^{17} cm^{-2}, where roughening of the surface becomes noticeable. For fluences up to 10^{18} cm^{-2}, a ripple pattern develops, which is clearer for the Xe system. Up to this fluence, the surface roughness, σ, increases for both systems, whereas the respective characteristic wavelength of the ripple pattern remains mostly constant. Finally, for even higher fluences ($4{\cdot}10^{18}$ cm^{-2}), the pattern becomes more disordered, particularly for the Ar + Fe case, where a marked saw-tooth morphology develops along the ion beam direction (see surface profile in Fig. 1d). In the Xe system, in addition to the nanometer ripples, raised triangular regions appear [46-49]. The corresponding fast Fourier transforms (FFTs) for the large fluence condition (insets) evidence spots associated to the main ripple periodicity in the Xe system, whereas for the Ar + Fe one, just a single central spot is visible reflecting the disordered surface.

For the Fe system, at medium fluences, small structures form that are aligned along the ion beam direction instead of perpendicularly aligned ripples as in the Xe case. With increasing ion fluence, they display saw-tooth morphology and a short-range ordering, as observed in the FFT shown in the inset, with a hexagonal symmetry. Thus, a clear ripple pattern does not develop in contrast to the Xe system. Finally, Fig. 1d shows surface profiles along the ion beam direction for the three systems for the high fluence of $4{\cdot}10^{18}$ cm^{-2}. In the Xe case, the nanometer undulations of the ripples are visible. The small but sharper negative slopes that can be spotted are due to the long-wave triangular features. In the other two systems involving Fe ions or atoms saw-tooth morphology develops, being more marked in the co-deposited case. In both systems, the saw-tooth structures have a short, sharp, and negatively sloped side, i.e. a facet facing the incoming ion beam known as upwind side, and a longer positively sloped one termed as downwind side [50].

In Fig. S1, higher resolution AFM images at different irradiation stages for the Fe system are displayed. For the lowest fluence, relatively long structures along the perpendicular direction to the ion beam, akin to a ripple-like structure, are observed together with smaller, mostly rounded, structures. On the large elongated structures, incipient small structures are also observed to be forming. For $5{\cdot}10^{17}$ cm^{-2}, the elongated structures are less and shorter. In addition, the smaller structures start to develop a saw-tooth shape. This trend is enhanced upon further irradiation. Finally, the small structures become predominant and display a short-range hexagonal ordering, in agreement with the FFT data. Besides, the few remaining large vertical structures become rather large triangular ones oriented along the ion beam direction, reminiscent of those found on Si under prolonged irradiation with Xe^+ (see Fig. 1, top row).

Fig. 2 shows the $PSD_{||}$ evolution for the Xe (a), Ar + Fe (b), and Fe (c) systems, respectively. They share certain features for large k values such as α values larger than 1, as well as an initial anomalous behavior ($PSD_{||}$ shifting upwards with fluence [51]), while for larger fluences, the PSDs tend to overlap. Also, a clear peak appears associated with ripple morphology (Xe and Ar + Fe systems). This peak vanishes when the bombarded surface becomes rougher and more disordered (Fe and Ar +

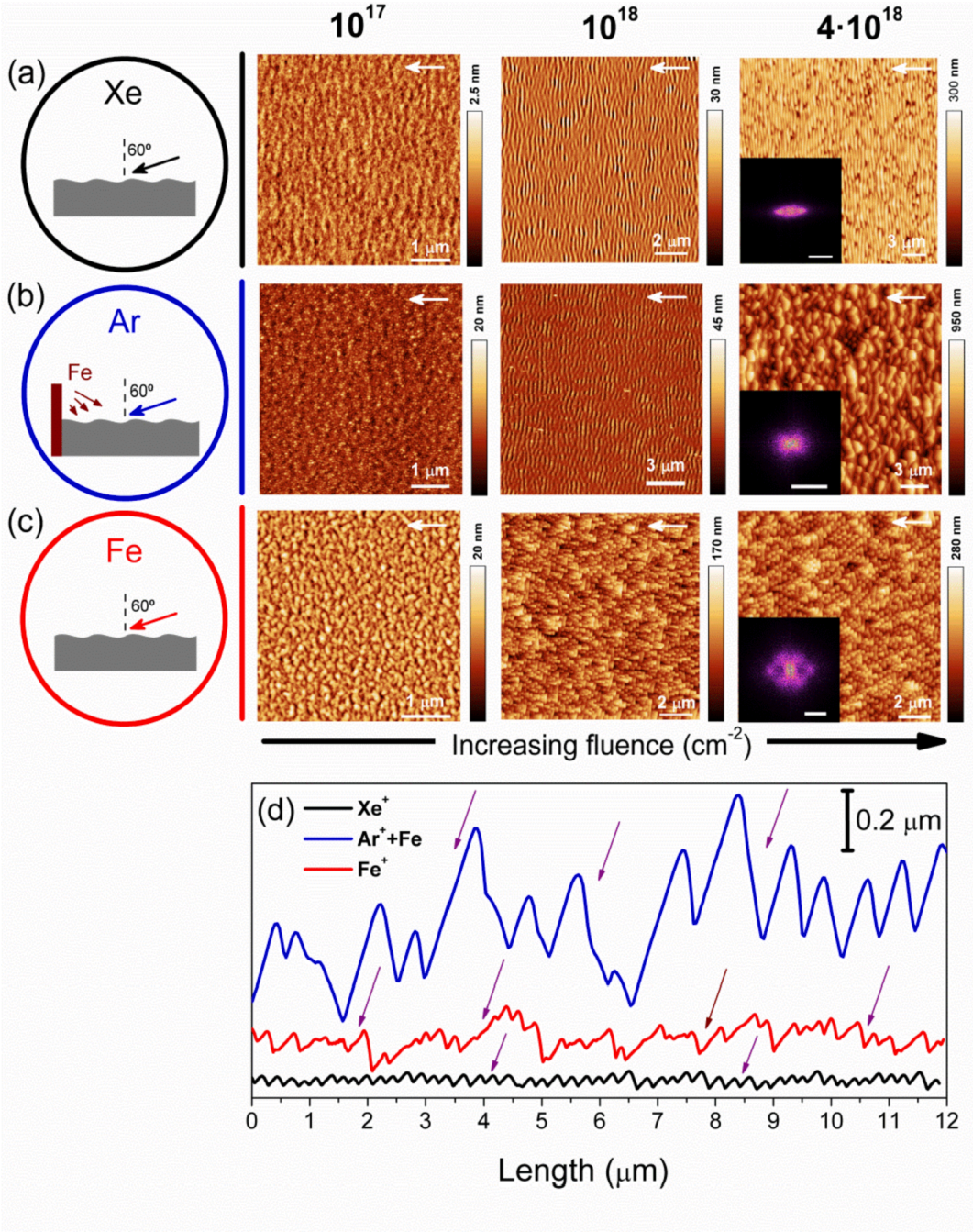

Fig. 1. AFM images for representative fluences for the two reference systems irradiated with 40 keV ions: (a) Xe^+, (b) Ar^+ with Fe co-deposition, and (c) Fe^+ ions. The arrows in the images indicate the beam direction. The insets are FFTs of the images and the scale bar is 5 μm^{-1}. The ion fluence is indicated at the top of each column. (d) Typical surface profiles along the ion beam projection direction of the three systems for a fluence of $4{\cdot}10^{18}$ cm^{-2}. The arrows indicate the real ion beam impact angle (note that in the plot, the vertical scale is enhanced). In the case of the Ar + Fe system, the Fe supply comes from the left.

Fe systems). The Fe system presents a particular feature since two values of α, 1 and 0.25, can be defined at large (short) and intermediate (medium) k (length) values, respectively. This new regime for medium k values is akin to the behavior observed for the Xe case. This correspondence is shown in the inset of Fig. 2c, as the $PSD_{||}$ for Xe shows a short new regime for $k < 10^{-3}$ nm^{-1} with a similar slope as that found for the Fe system.

Fig. 3a and 3b display the σ and λ evolution, respectively, for the three systems. Both systems involving Fe show a similar initial roughness evolution up to a fluence of 10^{18} cm^{-2} from which σ saturates for the Fe system while it keeps increasing for the Ar + Fe one. In contrast, for the Xe system, σ increases exponentially, although it seems to begin to saturate for the largest fluence. It should be noted that the roughening is faster for the Fe case than for the Xe one. In contrast, in terms of wavelength evolution, the Fe and Xe systems are rather similar since both show an initial increase of λ to reach a sort of saturation regime, with λ in the 200–300 nm range, at a fluence of 10^{17} cm^{-2}. Furthermore, this similarity is also observed for their λ values (filled symbols) associated with the second regime at smaller k values (see Fig. 2).

In contrast, although, up to 10^{18} cm^{-2}, the λ evolution for the Ar irradiation with co-deposition follows a similar behavior, for larger fluences, λ increases sharply to reach saturation at $\lambda \sim 1200$ nm.

Fig. 3c-e show the 2D slope distribution for the three systems. In all cases, the distribution is mostly elongated along the horizontal axis,

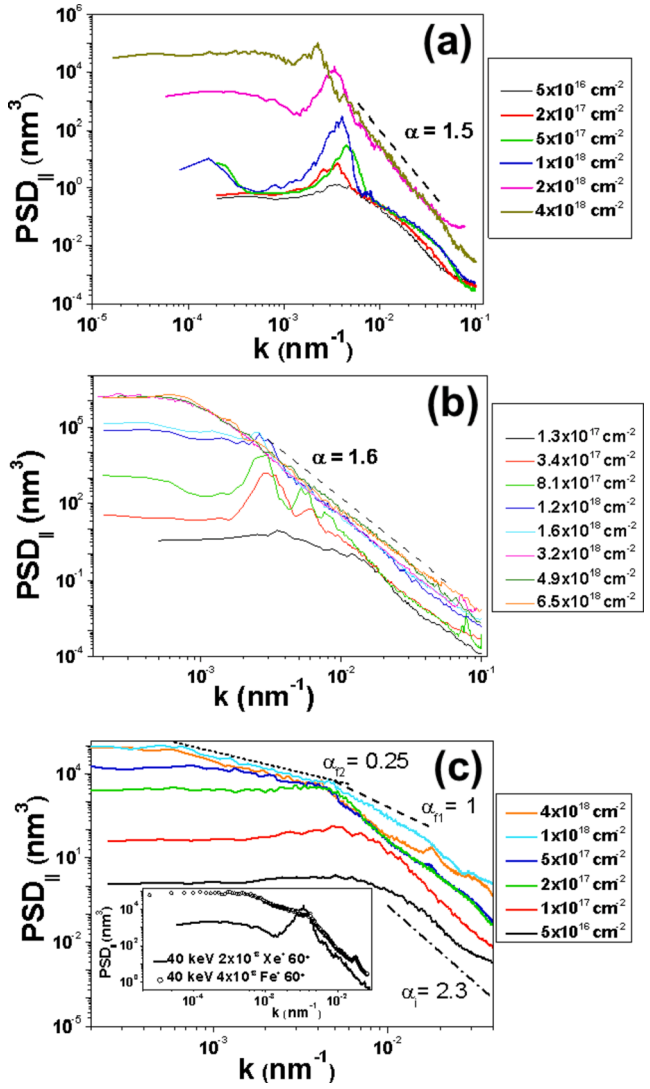

Fig. 2. Plot of the $PSD_{||}$ evolution with ion fluence for the Xe (a), Ar + Fe (b) and Fe (c) systems. The corresponding α values and ranges (dashed lines) are indicated for the low and high ion dose stages. (c) Inset: Plot of the $PSD_{||}$ curves for the Xe ($2x10^{18}$ cm^{-2}) and Fe ($4x10^{18}$ cm^{-2}) systems.

which is that of the projected ion beam direction. It is narrower for the Xe case, whereas for both Fe systems it is more spread in the x-y plane due to the more disordered and rougher induced morphology. The corresponding insets show the slope distribution along the x-axis (white lines). A marked peak is found with a positive slope that corresponds to that of the upwind ripple sides. In addition, for the Xe and Ar + Fe systems, a smaller peak with a negative slope is also found, which is due to the downwind ripple sides. These features correspond either to the ripple or to the saw-tooth morphologies induced for large fluences (see Fig. 1d).

3.2. Compositional evolution

From the previous analysis, it is clear that the incorporation of Fe atoms/ions on the bombarded Si surface induces marked changes on the pattern properties. Therefore, it is necessary to know the relevance of this incorporation with fluence, especially in the systems involving Fe supply during irradiation. This characterization was done by RBS/C (see figure S2). Fig. 4 plots the atomic content for Fe and Xe (as reference) extracted from the spectra.

In the case of single ion irradiation, the Xe content is constant in the whole fluence range, in qualitative agreement with simulations for low-energy Xe ion beam irradiation [52]. In contrast, for the Fe case, the metal content saturates for fluences higher than $5{\cdot}10^{17}$ cm^{-2}, indicating that the steady state is reached (both erosion and implantation rates are balanced). The final saturation level for Fe is close to $3{\cdot}10^{16}$ atoms/cm^2, one order of magnitude higher than the Xe content (which remains essentially constant even for low fluences). This comparison shows that there is a gradual enrichment of Fe in comparison to Xe.

In contrast, the Fe content in the case of co-deposition rises monotonously, reaching values as high as 10^{18} atoms/cm^2. It should be noted that for the Ar + Fe case, more than 5 Fe atoms per Ar^+ ion are sputtered away from the adjacent Fe plate and eventually land on the Si target. This fact could explain partially the higher Fe content than in the Fe^+ case.

3.3. Compositional spatial distribution

From the above results, it is evident that the induced patterns become rather different with increasing fluence. Thus, it becomes necessary to investigate how the different ions (Xe, Fe, Ar) are distributed on the target surface. Accordingly, we have performed TEM analysis of representative samples (Fig. 5) with relatively high fluences (10^{18} cm^{-2} and higher).

As a general feature of Fig. 5a-c, an amorphous silicon layer (a-Si, light-grey appearance compared to the darker single-crystalline Si substrate) is produced below the rippled surface. The thickness of this layer depends on the orientation. For the upwind side, facing the beam, the thickness is 48 nm (Xe), 59 nm (Fe), and 115 nm (Ar), in good agreement with the ranges obtained from SRIM simulations. In contrast, for the downwind ripple side, values of 20 nm (Xe), 25 nm (Fe), and 92 nm (Ar) are obtained. Thus, the upwind side is significantly thicker than the downwind side, since it suffers the direct implantation of the ion beam and, in addition, there is an additional sputtering due to the reflected ions [50,53].

The underlying amorphous-crystalline (a-c) interface also evidences a ripple pattern with a noticeably shift, which is close to 50 nm along the projected ion beam direction. This fact has been reported, at low and medium ion energies, and it is indeed a universal feature in ripple patterning [54-56]. Note that both sides of the surface ripple structure, upwind and downwind, run parallel to the corresponding ones in the a-c pattern too.

Concerning the spatial distribution of the elements at the surface, Fig. 5d shows a single ripple of the Xe-irradiated sample. The main feature observed here is the aggregation of Xe ions in the form of small bubbles, which are more evident in the element distribution map (inset). The size of these bubbles decreases with depth, a fact that has been reported in similar systems [54].

Fig. 5e shows the zoom of a Fe-irradiated structure with a fluence of $4{\cdot}10^{18}$ cm^{-2}. A clear saw-tooth pattern is observed, with asymmetric sides and, correspondingly, different thickness of the a-Si layers. The upwind side has evident Fe-rich (dark) agglomerates, also confirmed by element mapping (inset). The agglomerates are as thick as 40 nm, indicating the clustering of Fe at the upwind sides. It is worth to note that the Fe clusters are shifted towards the upwind side with respect to the ripple edge. In contrast, the downwind sides are almost free from Fe (except a thin surface layer) and also display a sloped morphology. Consequently, this sort of irradiation produces, not only a morphological pattern, but also a compositional one and both are not exactly in phase as the silicide regions lie, to some extent, centered on the upwind sides.

Fig. 5f shows the TEM image corresponding to a sample irradiated with Ar at a very high fluence ($6.5{\cdot}10^{18}$ cm^{-2}). Here, even more marked saw-tooth morphology is observed. However, due to the co-deposition, the Fe-rich domains are found on the downwind sides, i.e., those facing the metal source. In contrast, the upwind sides facing the Ar beam display quite scarce Fe domains or even none (see ref. [25] for a detailed discussion). Thus, in the Ar + Fe system, a compositional pattern is

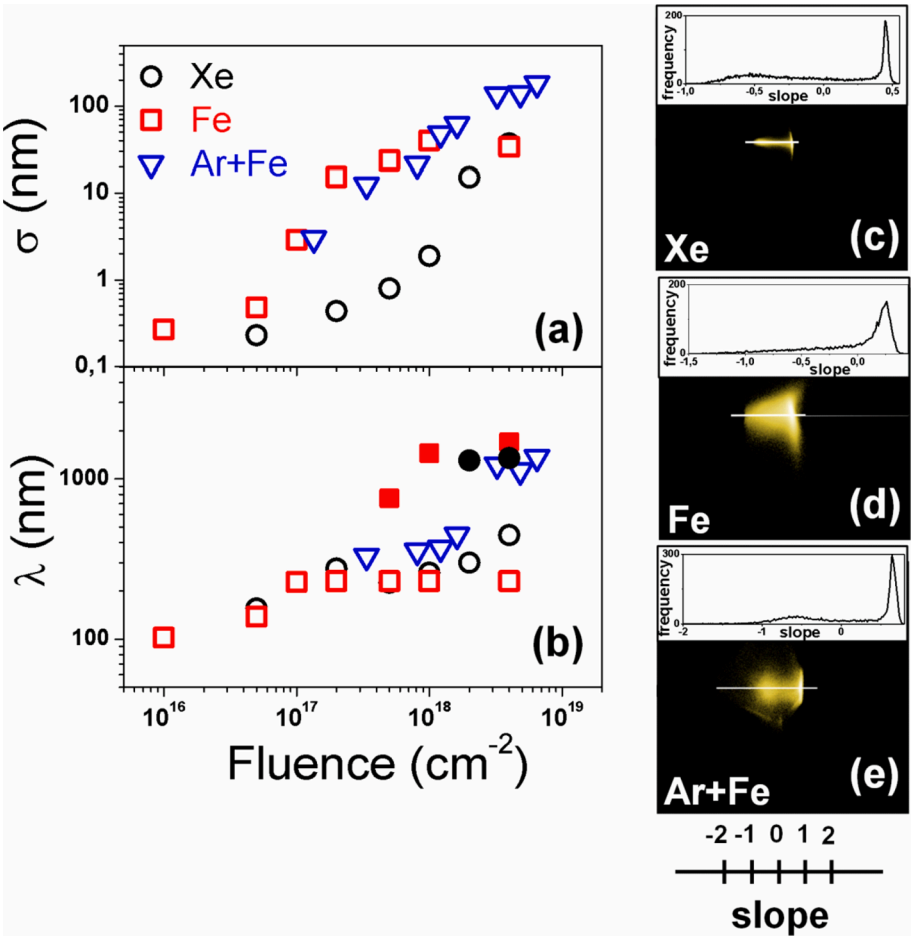

Fig. 3. (a) Roughness and (b) wavelength of the patterns for the three systems as indicated. Note the logarithmic scale in both graphs. In (b), the filled symbols correspond to the wavelength of the second regime. The error bars are not depicted for clarity sake. In the case of the roughness values, they are in the 10%-15% range, being smaller than the symbol size, whereas for the λ ones the error is close to 20%, and lies slightly above the top of the symbol in some cases. (c-e) Logarithmic 2D slope distribution of the samples irradiated at $4{\cdot}10^{18}$ cm^{-2} in the Xe, Fe, and Ar + Fe systems. The main bright stripe (at positive slopes) corresponds to the side facing the beam. Top insets: Plot of the slope distribution along the white line.

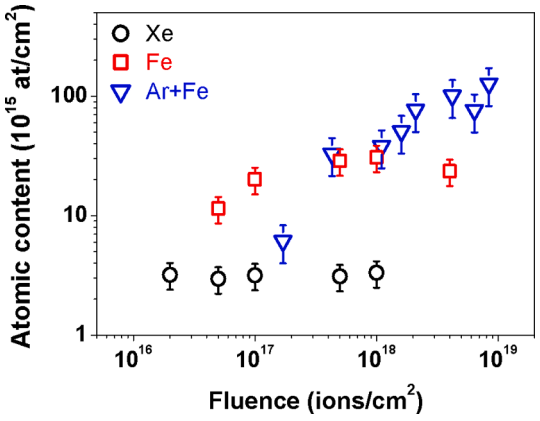

Fig. 4. Evolution of the atomic content of Xe (no metal) and Fe (pure metal and metal co-deposition) extracted from RBS analysis.

developed together with the morphological one, as for the direct Fe irradiation, but this time with the opposite correlation between them. Likewise, both patterns are not in phase as the Fe-rich regions lie on the downwind sides. An analogous behavior was reported for a fused silica target with a similar setup where its surface was irradiated with 500 eV Ar^+ ions and concurrent co-deposition of molybdenum [26]. Two more features are worth to be commented: (i) this time, the lateral shift of the maximum of the a-c saw-tooth structure is not related to the overlying Fe aggregate, and (ii) the bottom part of the upwind sides of the surface saw-tooth morphology is, in some cases, concave, which is likely related to enhanced erosion due to sputtering by reflected ions [50].

In order to further confirm the existence of these compositional patterns and their relationship with the corresponding morphological one, we have performed CS-AFM measurements. As reported previously [21,25], the current peaks take place at Fe-rich locations. Fig. 6 shows the topographic (a,d) and current (b,e) images for the two systems with metal incorporation. In the case of direct Fe irradiation, the current signal is high for the upwind side (Fig. 6b), whereas in the Ar + Fe system (Fig. 6e), the current is correlated with the downwind side of the saw-tooth morphology, i.e. those facets facing the Fe source. To better show this correlation Fig. 6c and 6f display superimposed topography and current profiles taken along the lines depicted in Fig. 6a,b and 6d,e, respectively. In both cases, it is clear that the high-current regions are those facing the Fe supply direction. These results are totally consistent with the TEM findings.

The TEM and CS-AFM analyses are rather local. In contrast, XPS can provide data on the Fe compositional pattern with higher statistical relevance for the surfaces subjected to large ion fluences, with clear saw-tooth morphology along the projected ion beam direction. This can be done by obtaining the atomic Fe/Si ratio of the surface from XPS spectra (not shown) as a function of the emission take-off angle. By tilting the sample with respect to the plane defined by the surface normal and the direction perpendicular to the projected ion beam (i.e., that one along the saw-tooth pattern), the upwind (downwind) sides will be mostly facing the detector for negative (positive) tilt angles. If a compositional pattern is produced, the Fe/Si ratio should change with the sign of the tilt angle. This is what happens for both systems involving Fe (Fig. 7). The change of composition with the tilt angle is very clear for the Ar + Fe system as the Fe/Si atomic ratio at the most negative tilt (−75°) is only the 10% of the maximum value obtained at the most positive tilt (+75°).

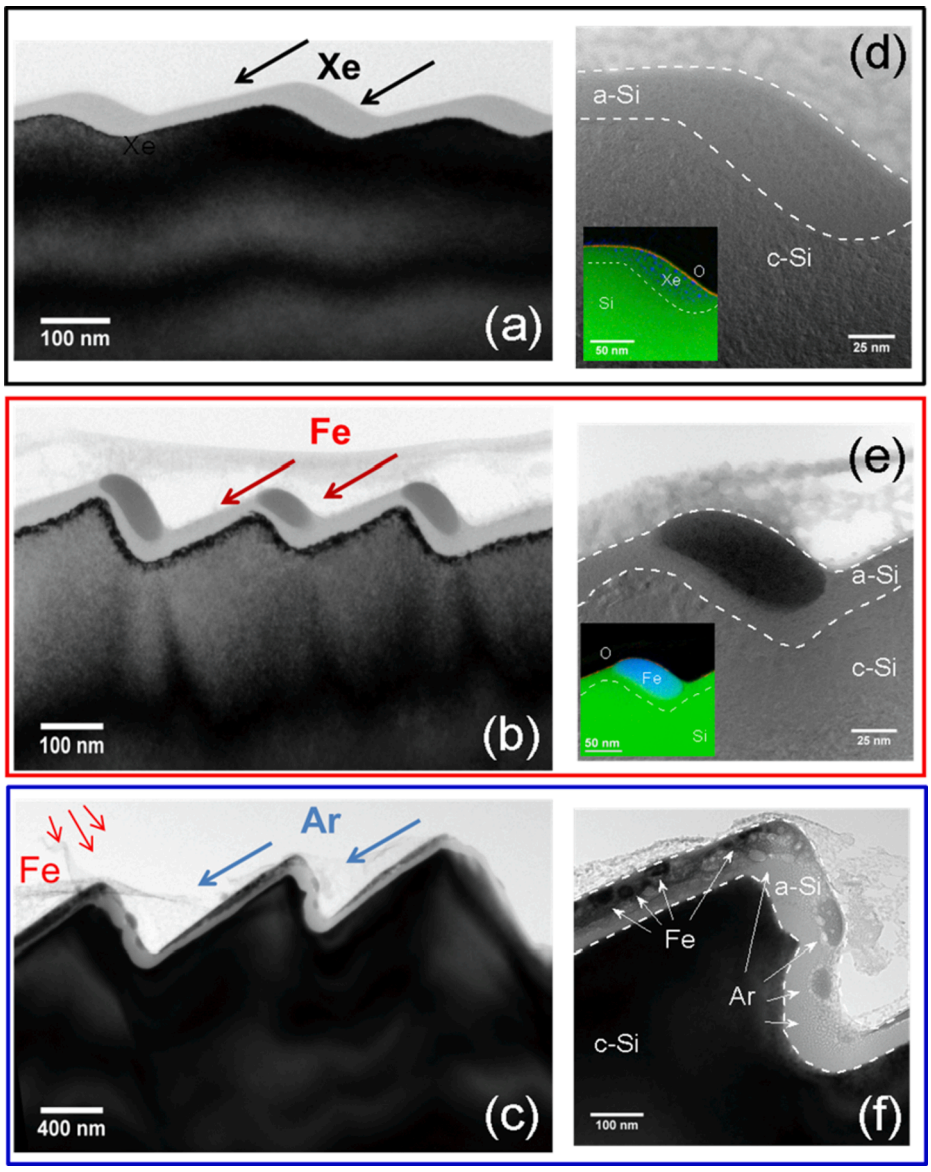

Fig. 5. Bright-field TEM images of representative samples for the (a) Xe (10^{18} cm^{-2}), (b) Fe ($4{\cdot}10^{18}$ cm^{-2}) and (c) Ar + Fe ($6.5{\cdot}10^{18}$ cm^{-2}) systems. Higher magnification images are shown in panels (d-f). Insets in images (d) and (e) displays the corresponding element distribution maps, where Si (green), Fe or Xe (blue) and O (red) signals are indicated.

This behavior agrees with the TEM and CS-AFM data.

The change in composition with tilt angle is not so marked for the Fe system since the minimum Fe/Si ratio, measured for +60° is the 40% of the maximum value measured at −60°. This different behavior can be due to the fact that the surface roughness of the Fe system is around 5 times smaller than that measured for the Ar + Fe system (Figs. 1-3), and, consequently, the eventual shadowing effects with respect to the XPS detector associated to the tilting geometry are lower than for the Ar + Fe system. Furthermore, the Fe-rich domains are quite localized close to the apex of the saw-tooth profile (Fig. 5b) and are smaller in size than those of Fig. 5c. These two facts, together with the lower Fe content of the Fe sample (around five times smaller than that of the Ar + Fe sample, see Fig. 4), indeed are related to the larger error bars of the Fe system compared to the Ar + Fe one. However, despite these facts, the increment of the Fe/Si ratio when tilting from positive to negative angles is consistent with the Fe-rich composition of the upwind sides of the saw-tooth pattern. Note, also, that the opposite dependence of the Fe/Si ratio with the tilting angle is a consequence of the different correlation between the morphological and chemical (silicide) patterns.

3.4. *In-depth chemical analysis*

Profiting from the large escape depth of high-kinetic-energy electrons [57], we have performed an in-depth chemical profile analysis by means of HAXPES. Fe1s, Si1s, and Fe2p core levels were probed using excitation energies of 9, 10.5, and 14 keV. The electron kinetic energy was varied between 1.9 keV and 13.3 keV corresponding to a depth analysis between 5 and 50 nm. Fig. 8a,b show the normalized HAXPES spectra for the Fe and Ar + Fe samples, respectively. The Fe2p and Fe1s spectra were aligned with respect to their main peak and normalized in intensity for better visualization and comparison. Interestingly, the spectra for the Fe sample present a single contribution, while the spectra for the Ar + Fe system display an additional emission at 3.6 eV from the main peak. The intensity for the second contribution decreases for higher electron kinetic energies. Although some studies can be found in the literature concerning the Fe1s and Fe2p HAXPES spectra for iron oxides [58], they are very scarce for iron silicides. According to the work by Badía-Romano et al. [59], the Fe1s HAXPES spectra for iron silicide compounds are dominated by the Fe(0) contribution together with a

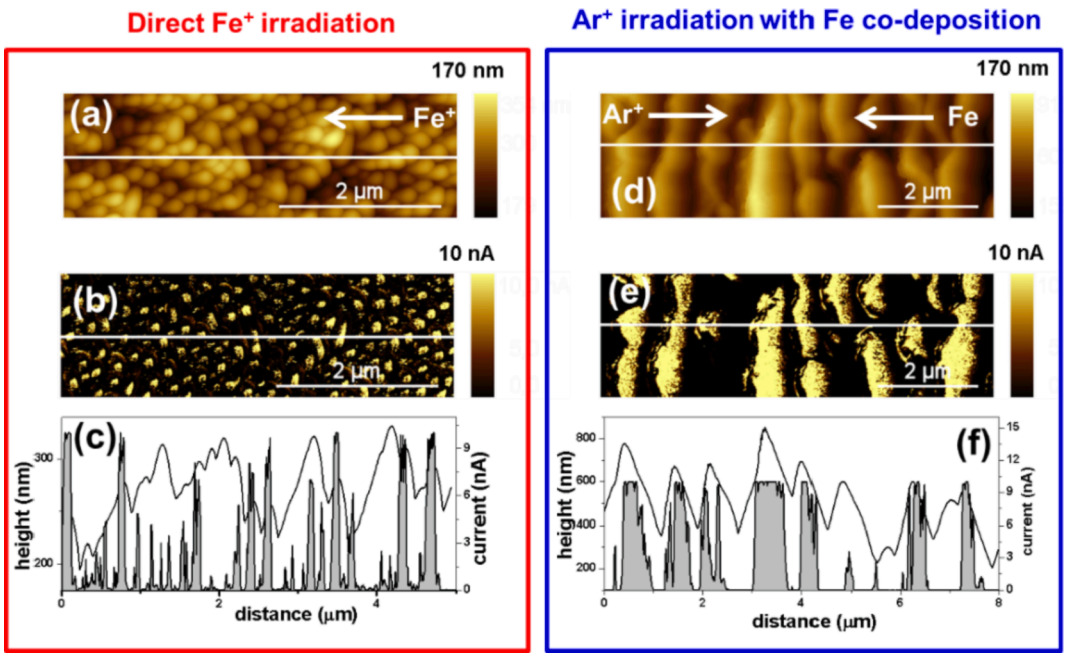

Fig. 6. AFM images of samples irradiated with (a-c) Fe and (d-f) Ar beams. (a,d) correspond to topography images, while (b,e) correspond to the equivalent current images. (c,f) are the cross-sectional profiles along the solid lines drawn in the respective topography and current images. The curves corresponding to the current profiles are the shaded ones. In both systems, the current increases at the slopes facing the Fe supply, indicating the formation of the compositional pattern.

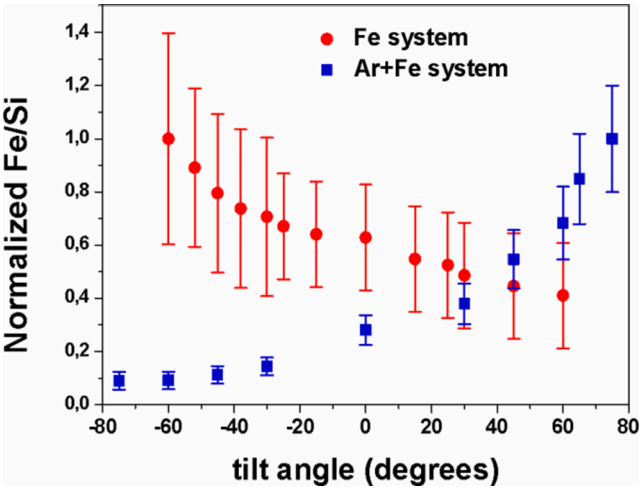

Fig. 7. Normalized Fe/Si atomic ratio measured by XPS for the samples irradiated with 4×10^{18} cm^{-2} for the Ar + Fe (blue filled squares) and Fe^{+} (red filled circles) systems, as a function of the emission take-off angle of the surface with respect to the detector. The samples have been tilted with respect to the axis perpendicular to the facetted pattern wavevector.

second contribution shifted by 1.2 eV. Chemical shift surface intrinsic energy loss portions appear above 5 eV. In the present case, by comparison with an iron reference sample exposed to air –see Fig. S3-, the contribution located at 3.6 eV is associated to surface contamination in the form of oxides, hydroxides and carbides, which is in good agreement with the results shown in [58]. Such a contribution is more intense for low electron kinetic energies due to the lower escape depth, while it is almost completely diminished for higher electron kinetic energies, i.e., higher sample depth. Hence, the comparison between both samples reveals the absence of surface contamination for the sample implanted with Fe ions while an iron contaminated layer of the order of 20 nm occurs for the sample sputtered with Ar and Fe co-evaporation. This is consistent with the different production dates of the samples, being the Ar + Fe one considerably older.

In addition, it can be inferred the presence of silicon oxide in the Fe and Ar + Fe samples. The analysis of the Si1s HAXPES spectra shown in Fig. 8c,d clearly shows the emission of a second contribution shifted by + 3.6 eV with respect to the main Si(0) peak, whose binding energy value is characteristic of silicon oxide. This contribution, which is larger for the Ar + Fe sample, decreases for both samples as the electron kinetic energy increases, which is representative of a surface oxide layer.

An insight into the stoichiometry distribution as a function of depth has been obtained by comparison of the absolute Fe2p and Si1s HAXPES intensities as a function of the photoelectron kinetic energy normalized by their respective photoemission cross-section [60]. Fig. 9 shows the trends for the Fe and Ar + Fe samples. An Fe:Si ratio of 1:1 is obtained for the Fe sample for the complete depth probed by the HAXPES technique, while a variable Fe:Si stoichiometry is found for the Ar + Fe sample. The latter sample shows a smooth variation from an Fe-rich surface with a Fe:Si ratio close to 4:1 up to a ratio of 3:1 for larger depths. The results for the Fe system contrast, at a first comparison, with those reported by Khanbabaee et al. [31] where a Si target was implanted with a 5 keV Fe^{+} ion beam impinging at $\theta = 65°$, and also analyzed by HAXPES. In their study, they found a silicide composition changing from Fe-rich (Fe_3Si) close to the surface to Si-rich ($FeSi_2$) towards the inner interface to the Si substrate. However, it is worth noting that their maximum excitation energy was almost one order of magnitude smaller than the minimum one employed in our study. Consequently, the range of sampled depth in that study was smaller (around 3.5 nm) than in the present case. It is important to note that Khanbabaee et al. [31] did find by XPS and X-ray absorption spectroscopy a progressive Si-enrichment of the silicide stoichiometry within their narrow depth range. Thus, our results showing a rather constant FeSi stoichiometry (i.e. Si-rich) with considerable larger sampled depths would be consistent with those reported in [31]. Notwithstanding, we have to stress that these quantifications can be quite affected by the marked saw-tooth morphology and surface roughness [61,62]. It should be noted that the saw-tooth morphologies in both cases have amplitudes close to or even larger than the depth sampled. In addition, the samples display a heterogeneous metal distribution both in-plane and in-depth. Therefore, the quantification must be considered rather as an indication of the

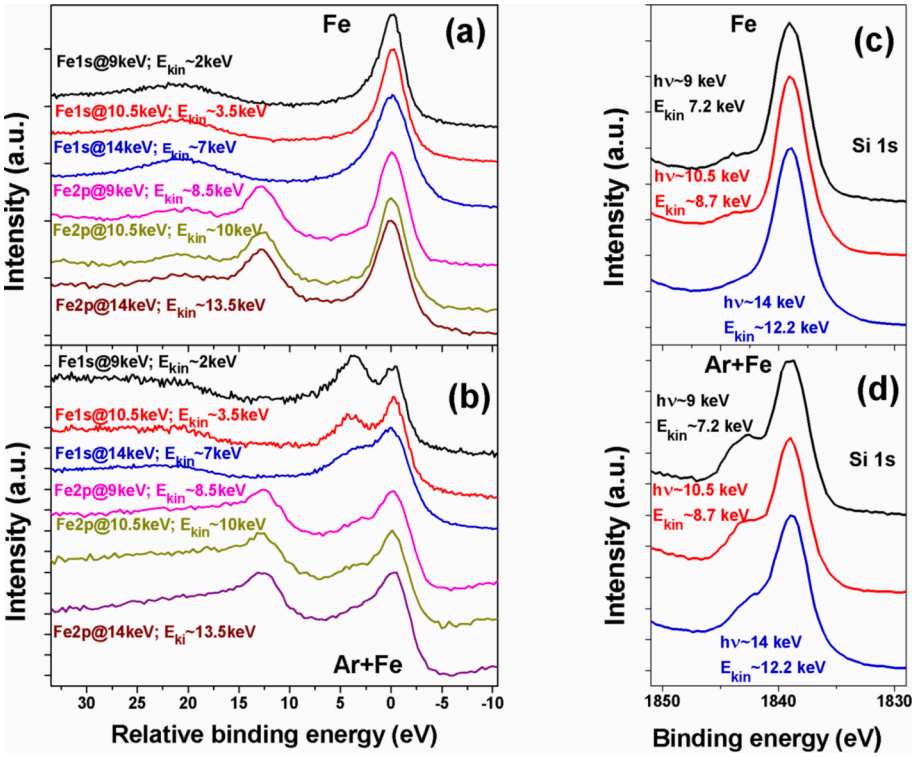

Fig. 8. Normalized HAXPES Fe1s and Fe2p spectra at different E_{kin} values for Fe (a) and Ar + Fe (b) samples; Si1s HAXPES spectra at different E_{kin} values for Fe (c) and Ar + Fe (d) samples.

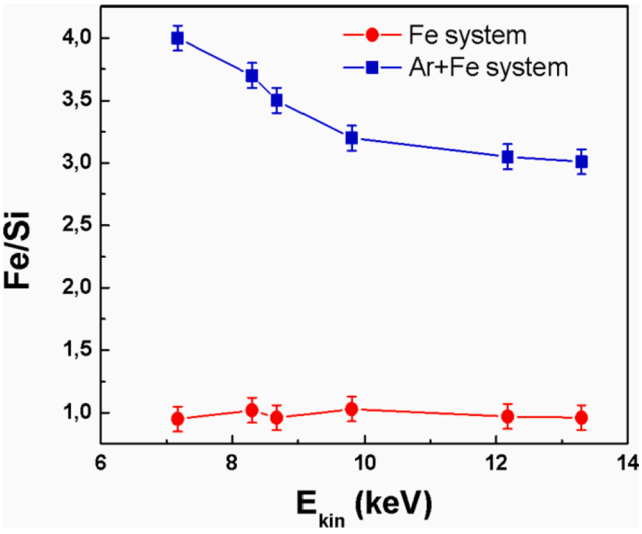

Fig. 9. Fe:Si ratio, obtained for the Fe and Ar + Fe systems by comparison of the absolute Fe2p and Si1s HAXPES intensities, as a function of the photoelectron kinetic energy normalized by their respective photoemission cross-section.

metal content variation.

3.5. Magnetic properties

The magnetic characterization of the samples is shown in Fig. 10a,b where the 4 K isotherm magnetization for the Ar + Fe and Fe samples is displayed. As expected, the saturation magnetization and the remanent magnetization increase with the fluence in both cases (Figs. S4a-c).

However, all these values are systematically much higher for the Fe sample than for the Ar + Fe one, which points towards a more efficient implantation process in the first case. Note also that the direct implantation of pure metal leads to a more robust magnetism of the implanted phase rendering not only higher saturation and remanence values but also smaller coercive fields. A common feature observed in both samples, is the non-monotonic dependence of the coercivity on the fluence (Fig. S4b). This could be related to the change from monodomain clusters produced at low and medium fluences to multi-domain large metallic patches obtained at higher fluences.

The high magnetic disorder of the co-deposited sample is also revealed in the irreversibility observed between the ZFC-FC temperature runs of the magnetization [63] shown in Fig. 11, bottom curve, as compared with that measured for the Fe sample displayed in Fig. 11, top curve.

In principle, these data indicate that the Fe sample shows better magnetic properties than the Ar + Fe one. This seems in contradiction with the main FeSi stoichiometry detected by HAXPES that is not magnetic [64,65]. However, as noted above, its quantification becomes problematic for such rough and compositionally, in-depth and laterally, heterogeneous samples. In addition, as it has been reported [65], small amounts of, for instance, Fe_3Si segregations can lead to a significant magnetic response, particularly with a technique with a high sensitivity as it is SQUID.

4. Discussion:

The obtained data allow to compare the IBS patterning of Si with a noble gas ion beam with that produced with Fe ions for $\theta = 60^\circ > \theta_{th}$. Both patterning processes differ in important aspects. When Xe ions are employed, ripple morphology develops that leads to a clear peak in the $PSD_{||}$. In contrast, for the Fe case, no rippling takes place but rather a saw-tooth morphology forms. Moreover, in this case, upon large fluence irradiation, the pattern symmetry is, although poorer, akin to the hexagonal one observed for Si surfaces irradiated normally by Xe^+ ions with isotropic metal co-deposition [14]. Another marked difference refers to the implanted regions: whereas Xe is found forming nanometer-sized

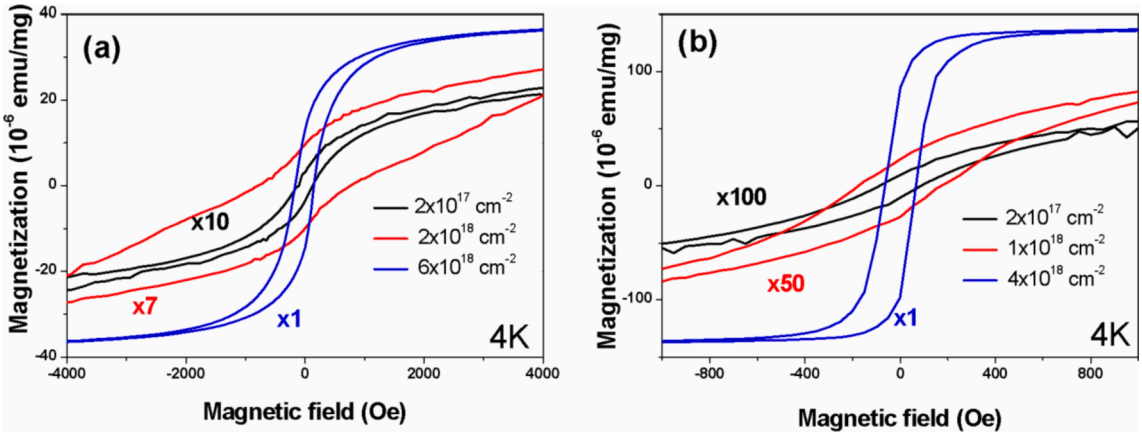

Fig. 10. Hysteresis cycle loops measured for the Ar + Fe (a) and Fe (b) samples at 4 K. Fluences are indicated.

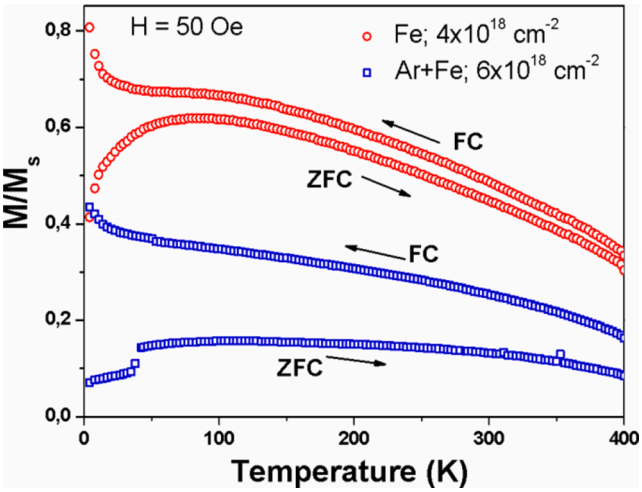

Fig. 11. ZFC and FC measurements of the magnetization vs temperature for the Ar + Fe (bottom curve, open squares) and Fe (top curve, open circles) samples.

bubbles, Fe forms rather compact aggregates, almost 100 nm wide. In this case, Fe is forming a silicide as the XPS and HAXPES data show. Also, Fig. 4 displays an enrichment of Fe with ion fluence, whereas the Xe content remains constant. This indeed would indicate the existence of preferential sputtering effects. In fact, in the Fe system, the silicide-rich clusters, with a lower sputtering yield, lead to a smaller shift between the peak of the surface ripple and that of the underlying (a-c) interface compared to the other two systems where noble gas ions impinge on the surface (see Fig. 5). These differences in the spatial ion implantation could have implications on the destabilizing effects associated with the increase in volume due to the implantation for large incidence angles [24] and, therefore, on the pattern evolution.

However, despite these marked differences between both systems, there are also some similarities. Thus, both systems present similar coarsening processes. For instance, note how in the inset of Fig. 2c the $PSD_{||}$ peak for the Xe system occurs at a k value close to the crossover between the first and second regimes in the Fe case, which is associated to the small structures (Fig. S1). This consistency in λ is surprising because the ion mass plays an important role on IBS patterning through the ion collision cascade [66,67]. Furthermore, for the Fe system chemical effects can arise that may boost the pattern development [15,16,21], which is consistent with its faster roughening compared to the Xe system. Another similarity is related to the second regime observed in the PSD for small k values and high fluences (Fig. 2). In the Xe case, this zone may be related to the large triangles that appear when non-linear effects operate (Fig. 1a) [48]. For the Fe system, they could be related to the large triangular-like structures that appear for large fluence.

The main interest of this work, however, lies on the study of the influence of the Fe pathway supply, either as ions (Fe system) or atoms (Ar + Fe system), on the pattern properties. Despite the different metal pathways, both systems have also some similarities. One of them is the likeness of their roughening processes, up to fluences close to 10^{18} cm^{-2}, despite their different pattern morphologies (Fig. 1,3). This roughening is faster than in the Xe case, likely because of the Si preferential sputtering effects induced by the silicide formation. Other likeness refers to the saw-tooth morphology that leads to wider slope distributions (Fig. 3) and the corresponding absence of a peak in the $PSD_{||}$.

However, the opposite Fe incorporation pathway for both systems triggers the marked differences that are observed, particularly for fluences higher than 10^{18} cm^{-2} where various parameters of the Ar + Fe pattern undergo a sharp change, as observed in Fig. 2b, 3a, 3b and 4b. So, σ and λ increase abruptly from their previous level, which is the one also attained for the Fe system. In parallel, the Fe content increases, too. In contrast, these parameters reach a steady state with ion fluence for the Fe system.

The observed behavior for the Ar + Fe case is a consequence of the Fe lateral supply. This pathway causes the Fe accumulation mainly on the downwind ripple side forming a silicide-rich side that has a lower sputtering yield (Figs. 5-7). In addition, the ion beam impacts on this side almost at grazing incidence, which also contributes to the lower sputtering yield. As this process proceeds the overall Fe content increases (Fig. 4b) and the saw-tooth morphology develops leading to enhanced roughening and coarsening (Fig. 3). Eventually, a scenario is attained where shadowing effects dominate the pattern dynamics. In this situation, the downwind side is impacted by the ions only at grazing incidence (Fig. 1d). Therefore, Fe still accumulates at this side while it cannot deposit on the upwind side. Likewise, the Ar ions mainly impinge on the upwind side. Consequently, a compositional pattern with Fe-rich downwind sides is produced, which would explain the Fe-rich silicide stoichiometry observed by HAXPES.

In contrast, in the Fe system, the Fe^+ beam impacts mainly on the upwind side of the ripple, sputtering away part of the Fe atoms already implanted. Thus, a steady-state is reached and the Fe content remains constant. This accumulation of Fe in the form of silicide lowers the sputtering yield locally and, consequently, saw-tooth morphology emerges. However, in this case, shadowing effects do not operate, which causes σ, λ and the Fe content to saturate. Moreover, a compositional pattern develops, but this time, with the upwind side of the saw-tooth pattern silicide-rich. The different Fe pathway supply also leads to different silicide compositions (Fe-richer for the Ar + Fe system) within the depth range sampled. Likewise, the silicide pattern formed by direct

Fe^+ implantation show better magnetic properties than the corresponding Ar + Fe one.

The formation of well localized silicide regions close to the saw-tooth edge obtained for the Fe system is quite similar to that obtained when a 36 keV Fe^+ ion impinged at 60° on a previously ripple patterned Si surface [32]. In fact the TEM images of both systems are quite similar. In that case the ripple pre-patterning was left to progress until a saw-tooth morphology developed. In contrast, in the present case, both the morphological and chemical patterning develop simultaneously. As figure S5 shows, MFM imaging of the Fe system for a high fluence condition shows magnetic nanostructures corresponding to the morphological pattern and hinting short-range hexagonal ordering.

The patterns obtained on Si surfaces with a Fe^+ ion beam differ from those obtained with a 26 keV Au^+ beam with $\theta = 60°$, where patches of ripples with two distinct wave vectors are produced [27]. Moreover, they also differ from the patterns induced by the same ion beam conditions on other mono-element flat semiconductors, such as Ge, for which extremely ordered ripple patterns were induced [27-29]. The most striking difference is, from the compositional point of view, that Au was found to decorate the ridges of the pattern when, from TRIM simulations, its sputtering yield is higher than that of Ge [28,29]. In this case, Au does not react with Ge, in contrast to the Fe system where it forms a silicide and accumulates at the upwind side of the saw-tooth morphology due to its lower sputtering yield.

However, the most surprising morphological result is the formation of a pattern with short-range hexagonal ordering in the Fe system. This feature contrasts with the ripple patterns obtained under oblique incidence, provided that $\theta < 80°$, for which the wave vector is oriented along the projected ion beam direction [50]. As mentioned above, to some extent, this short-range hexagonally ordered pattern resembles the dot patterns obtained for normal ion incidence with isotropic metal co-deposition [13,14]. However, in the present case, the structures form a rather compact pattern, whereas in the co-deposited cases there are flat regions between dots. Among the different mechanisms that could contribute to destabilize the surface to yield a pattern, neither the mass surface redistribution effects, nor the erosive one [68], nor the implantation contribution [24] yield an eventual instability along the perpendicular direction to the projected ion beam direction. Viscous flow could, under certain conditions, lead to a certain destabilizing contribution along the perpendicular direction [69]. Another possibility, hinted in a previous report [70], comes from the fact that on the downwind sides of the saw-tooth structures the ion beam impacts the surface close to grazing incidence for which perpendicular-mode roughening dominates pattern formation.

5. Conclusions:

We have produced patterns on silicon by 40 keV ion bombardment at an oblique incidence angle of 60° for three different systems, namely Fe^+, Xe^+ ions, as well as Ar^+ ions with a simultaneous Fe directional supply. For Fe^+ irradiation, saw-tooth morphological patterns develop together with a compositional one with Fe-rich zones, centered at the upwind sides, as confirmed by TEM, CS-AFM and XPS. A saw-tooth morphological pattern and a compositional one are also formed for Ar^+ irradiation with Fe co-deposition. However, in this case, the Fe-rich phase lies on the downwind side and marked shadowing effects come into play and determine the evolution of both patterns. While the Xe content is constant with increasing fluence, the metal content increases with fluence for both systems involving Fe, which is consistent with silicide formation and Si preferential sputtering process. The formation of silicide is confirmed by XPS and HAXPES. Despite the differences in the sputtering process, the pattern dynamics with Fe^+ ions share some features both with the Xe^+ system as well as with the co-deposited one. However, the main novelty in the Fe^+ case lies, for large enough fluences, in the development of a pattern displaying short-range hexagonal ordering, which differs greatly from the ripple pattern obtained under oblique incidence conditions. In addition, both Fe-containing systems develop a chemical pattern with silicide-rich and -poor regions. However, the correlation of the chemical pattern with the morphological one depends on the Fe pathway. Likewise, this pathway has strong influence on the magnetic properties of the surface pattern since the implanted one has better properties than the co-deposited one. Also, the silicide stoichiometry does depend on the metal pathway since the implanted system has a lower Fe:Si ratio than the co-deposited one. These results show that in ion-beam-induced silicon surface patterning with reactive metals, such as Fe, the pathway in which Fe is supplied onto the surface, either as an ion or co-deposited, is critical to determine the surface pattern properties.

CRediT authorship contribution statement

A. Redondo-Cubero: Methodology, Validation, Formal analysis, Investigation, Resources, Writing – review & editing, Funding acquisition. **F.J. Palomares:** Methodology, Validation, Formal analysis, Investigation, Resources, Writing – review & editing, Funding acquisition. **K. Lorenz:** Methodology, Validation, Investigation, Resources, Writing – review & editing. **J. Rubio-Zuazo:** Methodology, Validation, Formal analysis, Resources, Investigation, Writing – review & editing, Funding acquisition. **R. Hübner:** Methodology, Validation, Formal analysis, Investigation, Writing – review & editing. **F.J. Mompeán:** Methodology, Validation, Formal analysis, Investigation, Writing – review & editing. **M. García-Hernández:** Methodology, Validation, Formal analysis, Investigation, Writing – review & editing, Funding acquisition. **G.R. Castro:** Methodology, Validation, Formal analysis, Investigation, Writing – review & editing, Funding acquisition. **L. Vázquez:** Methodology, Validation, Formal analysis, Investigation, Writing – review & editing, Conceptualization, Supervision, Project administration, Funding acquisition.

Declaration of Competing Interest

The authors declare that they have no known competing financial interests or personal relationships that could have appeared to influence the work reported in this paper.

Acknowledgements

This research is supported by Spanish MINECO (Grant No. MAT2016-80394-R and No. PID2020-113142RB-C21) and the TRANSNANOAVANSENS program (Grant No.S2018/NMT-4349) from the Comunidad de Madrid. A.R.C. acknowledges Ramón y Cajal program (under Contract No. RYC-2015-18047). F.J.P. is thankful for financial support by A.E. Consejo Superior de Investigaciones Científicas (under Grant No. CSIC-2019AEP150). The use of the HZDR Ion Beam Center TEM facilities is gratefully acknowledged. We acknowledge the Spanish Ministerio de Ciencia e Innovación and Consejo Superior de Investigaciones Científicas for financial support -PIE 2010 6 0E 013 and PIE 2021 60 E 030- and for provision of synchrotron radiation facilities. We want to thank the operators of the SPLINE-BM25b beamline, and ESRF for the allocated beamtime (MA-2482, 25-02-849).We are grateful to M. Missbach for TEM specimen preparation as well as R. Cuerno, R. Gago, and E. García-Michel for useful discussions.

Appendix A. Supplementary data

Supplementary data to this article can be found online at https://doi.org/10.1016/j.apsusc.2021.152267.

References

[1] J. Muñoz-García, L. Vázquez, R. Cuerno, J.A. Sánchez-García, M. Castro, R. Gago, Self-Organized Surface Nanopatterning by Ion Beam Sputtering, in: Z.M. Wang

(Ed.), Toward Functional Nanomaterials, Springer US, New York, NY, 2009, pp. 323–398, https://doi.org/10.1007/978-0-387-77717-7_10.
[2] D. Chowdhury, D. Ghose, Nanoripple formation on GaAs (001) surface by reverse epitaxy during ion beam sputtering at elevated temperature, Appl. Surf. Sci. 385 (2016) 410–416, https://doi.org/10.1016/j.apsusc.2016.05.099.
[3] D. Bhowmik, D. Chowdhury, P. Karmakar, Dynamic scaling behavior of mica ripples produced by low energy Ar^+ ion erosion, Suf. Sci. 679 (2019) 86–92, https://doi.org/10.1016/j.susc.2018.08.016.
[4] J. Muñoz-García, L. Vázquez, M. Castro, R. Gago, A. Redondo-Cubero, A. Moreno-Barrado, R. Cuerno, Self-Organized Nanopatterning of Silicon Surfaces by Ion Beam Sputtering, Mater. Sci. Eng. R Rep. 86 (2014) 1–44, https://doi.org/10.1016/j.mser.2014.09.001.
[5] R.M. Bradley, J.M.E. Harper, Theory of ripple topography induced by ion bombardment, J. Vac. Sci. Technol., A 6 (1988) 2390–2395, https://doi.org/10.1116/1.575561.
[6] C.S. Madi, E. Anzenberg, K.F. Ludwig Jr., M.J. Aziz, Mass Redistribution Causes the Structural Richness of Ion-Irradiated Surfaces, Phys. Rev. Lett. 106 (2011), 066101, https://doi.org/10.1103/PhysRevLett.106.066101.
[7] G. Carter, V. Vishnyakov, Roughening and ripple instabilities on ion-bombarded Si, Phys. Rev. B 54 (1996) 17647–17653, https://doi.org/10.1103/PhysRevB.54.17647.
[8] M. Moseler, P. Gumbsch, C. Casiraghi, A.C. Ferrari, J. Robertson, The Ultrasmoothness of Diamond-like Carbon Surfaces, Science 309 (2005) 1545–1548, https://doi.org/10.1126/science.1114577.
[9] B. Davidovitch, M.J. Aziz, M.P. Brenner, On the stabilization of ion sputtered surfaces, Phys. Rev. B 76 (2007), 205420, https://doi.org/10.1103/PhysRevB.76.205420.
[10] C. Teichert, C. Hofer, G. Hlawacek, Self-organization of Nanostructures in Inorganic and Organic Semiconductor Systems, Adv. Eng. Mater. 8 (2006) 1057–1065, https://doi.org/10.1002/adem.200600142.
[11] K. Zhang, M. Brötzmann, H. Hofsäss, Surfactant-driven self-organized surface patterns by ion beam erosion, New J. Phys. 13 (2011), 013033, https://doi.org/10.1088/1367-2630/13/1/013033.
[12] S. Macko, F. Frost, M. Engler, D. Hirsch, T. Höche, J. Grenzer, T. Michely, Phenomenology of Iron-Assisted Ion Beam Pattern Formation on Si(001), New J. Phys. 1 (2011), 073017, https://doi.org/10.1088/1367-2630/13/7/073017.
[13] R. Gago, A. Redondo-Cubero, F.J. Palomares, L. Vázquez, Influence of Metal Co-Deposition on Silicon Nanodot Patterning Dynamics during Ion-Beam Sputtering, Nanotechnology 25 (2014), 415301, https://doi.org/10.1088/0957-4484/25/41/415301.
[14] A. Redondo-Cubero, B. Galiana, K. Lorenz, F.J. Palomares, D. Bahena, C. Ballesteros, I. Hernandez-Calderón, L. Vázquez, Self-Organised Silicide Nanodot Patterning by Medium-Energy Ion Beam Sputtering of Si(100): Local Correlation between the Morphology and Metal Content, Nanotechnology 27 (2016), 444001, https://doi.org/10.1088/0957-4484/27/44/444001.
[15] K. Zhang, M. Brötzmann, H. Hofsäss, Sharp Transition from Ripple Patterns to a Flat Surface for Ion Beam Erosion of Si with Simultaneous Co-Deposition of Iron, AIP Adv. 2 (2012), 032123, https://doi.org/10.1063/1.4739843.
[16] M. Engler, F. Frost, S. Müller, S. Macko, M. Will, R. Feder, D. Spemann, S. René Hübner, S. Facsko, T. Michely, Silicide Induced Ion Beam Patterning of Si(001), Nanotechnology 25 (2014), 115303, https://doi.org/10.1088/0957-4484/25/11/115303.
[17] K.S. Lloyd, I.L. Bolotin, M. Schmeling, L. Hanley, I.V. Veryovkina, Metal impurity-assisted formation of nanocone arrays on Si by low energy ion-beam irradiation, Surf. Sci. 652 (2016) 334–343, https://doi.org/10.1016/j.susc.2016.03.016.
[18] B. Moon, S. Yoo, J.-S. Kim, S.J. Kang, J. Muñoz-García, R. Cuerno, Ion-beam nanopatterning of silicon surfaces under codeposition of non-silicide-forming impurities, Phys. Rev. B 93 (2016), 115430, https://doi.org/10.1103/PhysRevB.93.115430.
[19] K. Zhang, O. Bobes, H. Hofsäss, Designing self-organized nanopatterns on Si by ion irradiation and metal co-deposition, Nanotechnology 25 (2014), 085301, https://doi.org/10.1088/0957-4484/25/8/085301.
[20] B. Ziberi, F. Frost, M. Tartz, H. Neumann, B. Rauschenbach, Ripple rotation, pattern transitions, and long range ordered dots on silicon by ion beam erosion, Appl. Phys. Lett. 92 (2008), 063102, https://doi.org/10.1063/1.2841641.
[21] A. Redondo-Cubero, F.J. Palomares, R. Hübner, R. Gago, L. Vázquez, Highly Ordered Silicide Ripple Patterns Induced by Medium-Energy Ion Irradiation, Phys. Rev. B 102 (2020), 075423, https://doi.org/10.1103/PhysRevB.102.075423.
[22] J. Zhou, M. Lu, Mechanism of Fe impurity motivated ion-nanopatterning of Si (100) surfaces, Phys. Rev. B 82 (2010), 125404, https://doi.org/10.1103/PhysRevB.82.125404.
[23] R.M. Bradley, Producing ripple topographies by ion bombardment with codeposition of impurities: A curvature-dependent sputter yield is not required, Phys. Rev. B 85 (2012), 115419, https://doi.org/10.1103/PhysRevB.85.115419.
[24] H. Hofsäss, K. Zhang, O. Bobes, Self-organized surface ripple pattern formation by ion implantation, J. Appl. Phys. 120 (2016), 135308, https://doi.org/10.1063/1.4964113.
[25] A. Redondo-Cubero, R. Gago, F.J. Palomares, A. Mücklich, M. Vinnichenko, L. Vázquez, Nanopatterning dynamics on Si(100) during oblique 40-keV Ar^+ erosion with metal codeposition: Morphological and compositional correlation, Phys. Rev. B 86 (2012), 085436, https://doi.org/10.1103/PhysRevB.86.085436.
[26] D. Chen, G. Yang, J. Li, D. Hirsch, Y. Liu, F. Frost, Y. Hong, Terrace morphology on fused silica surfaces by Ar^+ ion bombardment with Mo codeposition, Appl. Phys. Lett. 113 (2018), 033102, https://doi.org/10.1063/1.5039565.
[27] S.A. Mollick, D. Ghose, P.D. Shipman, R.M. Bradley, Anomalous patterns and nearly defect-free ripples produced by bombarding silicon and germanium with a beam of gold ions, Appl. Phys. Lett. 104 (2014), 043103, https://doi.org/10.1063/1.4863342.
[28] S.A. Mollick, M. Kumar, R. Singh, B. Satpati, D. Ghose, T. Som, Gold-decorated highly ordered self-organized grating-like nanostructures on Ge surface: Kelvin probe force microscopy and conductive atomic force microscopy studies, Nanotechnology 27 (2016), 435302, https://doi.org/10.1088/0957-4484/27/43/435302.
[29] R. Dell'Anna, E. Iacob, M. Barozzi, L. Vanzetti, R. Hübner, R. Böttger, D. Giubertoni, G. Pepponi, The role of incidence angle in the morphology evolution of Ge surfaces irradiated by medium-energy Au ions, J. Phys.: Condens. Matter 30 (2018), 324001, https://doi.org/10.1088/1361-648X/aacf5f.
[30] B. Khanbabaee, S. Facsko, S. Doyle, U. Pietsch, Near-Surface Density Profiling of Fe Ion Irradiated Si (100) Using Extremely Asymmetric x-Ray Diffraction by Variation of the Wavelength, Appl. Phys. Lett. 105 (2014), 163101, https://doi.org/10.1063/1.4899068.
[31] B. Khanbabaee, D. Lützenkirchen-Hecht, R. Hübner, J. Grenzer, S. Facsko, U. Pietsch, Near Surface Silicide Formation after Off-Normal Fe-Implantation of Si (001) Surfaces, J. Appl. Phys. 116 (2014), 024301, https://doi.org/10.1063/1.4887516.
[32] P. Karmakar, B. Satpati, Site specific isolated nanostructure array formation on a large area by broad ion beam without any mask and resist, Appl. Phys. Lett. 104 (2014), 231601, https://doi.org/10.1063/1.4881333.
[33] K.J. Kirk, Nanomagnets for sensors and data storage, Contemp. Phys. 41 (2000) 61–78, https://doi.org/10.1080/001075100181187.
[34] B.D. Terris, T. Thomson, Nanofabricated and self-assembled magnetic structures as data storage media, J. Phys. D: Appl. Phys. 38 (2005) R199–R222, https://doi.org/10.1088/0022-3727/38/12/R01.
[35] C.-C. Chang, K.W. Sun, S.-F. Lee, L.-S. Kann, Self-assembled molecular magnets on patterned silicon substrates: bridging bio-molecules with nanoelectronics, Biomaterials 28 (2007) 1941–1947, https://doi.org/10.1016/j.biomaterials.2006.11.048.
[36] T. Bobek, N. Mikuszeit, J. Camarero, S. Kyrsta, L. Yang, M.A. Niño, C. Hofer, L. Gridneva, D. Arvanitis, R. Miranda, J.J. de Miguel, C. Teichert, H. Kurz, Self-organized hexagonal patterns of independent magnetic nanodots Adv, Mater. 19 (2007) 4375–4380, https://doi.org/10.1002/adma.200701163.
[37] C. Teichert, J.J. de Miguel, T. Bobek, Ion beam sputtered nanostructured semiconductor surfaces as templates for nanomagnet arrays, J. Phys.: Condens. Matter 21 (2009), 224025, https://doi.org/10.1088/0953-8984/21/22/224025.
[38] J.J. de Miguel, T. Bobek, C. Teichert, Recent Patents on Self-Organised Magnetic Nanodot Arrays, Recent Pat. Nanotechnol. 5 (2011) 1–18, https://doi.org/10.2174/187221011794474958.
[39] D. Briggs, M.P. Seah, Practical Surface Analysis: Auger and X-Ray Photoelectron Spectroscopy, Wiley, New York, 1990.
[40] D. Nečas, P. Klapetek, Gwyddion: An Open-Source Software for SPM Data Analysis, Open Phys. 10 (2012) 181–188, https://doi.org/10.2478/s11534-011-0096-2.
[41] J. Muñoz-García, R. Gago, R. Cuerno, J.A. Sánchez-García, A. Redondo-Cubero, M. Castro, L. Vázquez, Independence of Interrupted Coarsening on Initial System Order: Ion-Beam Nanopatterning of Amorphous versus Crystalline Silicon Targets, J. Phys. Condens. Matter 24 (2012), 375302, https://doi.org/10.1088/0953-8984/24/37/375302.
[42] E. Vivo, M. Nicoli, M. Engler, T. Michely, L. Vázquez, R. Cuerno, Strong Anisotropy in Surface Kinetic Roughening: Analysis and Experiments, Phys. Rev. B 86 (2012), 245427, https://doi.org/10.1103/PhysRevB.86.245427.
[43] A. Redondo-Cubero, M.J.G. Borge, N. Gordillo, P.C. Gutiérrez, J. Olivares, R. Pérez Casero, M.D. Ynsa, Current status and future developments of the ion beam facility at the Centre of Micro-Analysis of Materials in Madrid, Eur. Phys. J. Plus 136 (2021) 175, https://doi.org/10.1140/epjp/s13360-021-01085-9.
[44] J.R. Rubio-Zuazo, G.R. Castro, Hard X-Ray Photoelectron Spectroscopy (HAXPES) (⩽15keV) at SpLine, the Spanish CRG Beamline at the ESRF, Nucl. Instrum. Methods Phys. Res. A 547 (2005) 64–72, https://doi.org/10.1016/j.nima.2005.05.013.
[45] J. Rubio-Zuazo, P. Ferrer, G.R. Castro, Non-Destructive Compositional Depth Profile in the Tens-of-Nanometer Scale, J. Electron Spectrosc. Relat. Phenom. 180 (2010) 27–33, https://doi.org/10.1016/j.elspec.2010.03.013.
[46] A. Keller, R. Cuerno, S. Facsko, W. Möller, Anisotropic Scaling of Ripple Morphologies on High-Fluence Sputtered Silicon, Phys. Rev. B 79 (2009), 115437, https://doi.org/10.1103/PhysRevB.79.115437.
[47] A. Keller, S. Facsko, Ion-Induced Nanoscale Ripple Patterns on Si Surfaces: Theory and Experiment, Materials 3 (2010) 4811–4841, https://doi.org/10.3390/ma3104811.
[48] K.M. Loew, R.M. Bradley, Effect of Dispersion on the Nanoscale Patterns Produced by Ion Sputtering, Phys. Rev. E 100 (2019), 012801, https://doi.org/10.1103/PhysRevE.100.012801.
[49] S. Hans, M. Ranjan, Emergence of triangular features on ion irradiated silicon (100) surface, Surf. Sci. 75 (2022), 121951, https://doi.org/10.1016/j.susc.2021.121951.
[50] M. Engler, S. Macko, F. Frost, T. Michely, Evolution of Ion Beam Induced Patterns on Si(001), Phys. Rev. B 89 (2014), 245412, https://doi.org/10.1103/PhysRevB.89.245412.
[51] M.A. Auger, L. Vázquez, R. Cuerno, M. Castro, M. Jergel, O. Sánchez, Intrinsic Anomalous Surface Roughening of TiN Films Deposited by Reactive Sputtering, Phys. Rev. B 73 (2006), 045436, https://doi.org/10.1103/PhysRevB.73.045436.
[52] M.A. Lively, S.X. Bennet, J.P. Allain, Molecular dynamics studies of ion beam implantation and patterning of silicon: Effect of noble gas cluster formation, Phys. Rev. B 97 (2018), 235443, https://doi.org/10.1103/PhysRevB.97.235443.

[53] W. Hauffe, Faceting Mechanism in the Sputtering Process, Phys. Status Solidi A 35 (1976) K93–K96, https://doi.org/10.1002/pssa.2210350246.
[54] T.K. Chini, D.P. Datta, S.R. Bhattacharyya, Ripple Formation on Silicon by Medium Energy Ion Bombardment, J. Phys. Condens. Matter 21 (2009), 224004, https://doi.org/10.1088/0953-8984/21/22/224004.
[55] S.K. Garg, D.P. Datta, J. Ghatak, S.R. Tripathy, D. Kanjilal, T. Som, Medium Energy Ar^{+}-Ion Induced Ripple Formation: Role of Ion Energy in Pattern Formation, Appl. Surf. Sci. 317 (2014) 476–479, https://doi.org/10.1016/j.apsusc.2014.08.128.
[56] A. Moreno-Barrado, M. Castro, R. Gago, L. Vázquez, J. Muñoz-García, A. Redondo-Cubero, B. Galiana, C. Ballesteros, R. Cuerno, Nonuniversality Due to Inhomogeneous Stress in Semiconductor Surface Nanopatterning by Low-Energy Ion-Beam Irradiation, Phys. Rev. B 91 (2015), 155303, https://doi.org/10.1103/PhysRevB.91.155303.
[57] J. Rubio-Zuazo, G.R. Castro, Information depth determination for hard X-ray photoelectron spectroscopy up to 15 keV photoelectron kinetic energy, Surf. Interface Anal. 40 (2008) 1438–1443, https://doi.org/10.1002/sia.2920.
[58] J. Rubio-Zuazo, A. Chainani, M. Taguchi, D. Malterre, A. Serrano, G.R. Castro, Electronic structure of FeO, γ−Fe_2O_3, and Fe_3O_4 epitaxial films using high-energy spectroscopies, Phys. Rev. B 97 (2018), 235148, https://doi.org/10.1103/PhysRevB.97.235148.
[59] L. Badía-Romano, J. Rubín, F. Bartolomé, C. Magén, J. Bartolomé, S.N. Varnakov, S.G. Ovchinnikov, J. Rubio-Zuazo, G.R. Castro, Morphology of the asymmetric iron–silicon interfaces, J. Alloys Compd. 627 (2015) 136–145, https://doi.org/10.1016/j.jallcom.2014.12.019.
[60] J.H. Scofield, Theoretical Photoionization Cross-sections from 1 to 1500 keV, Lawrence Livermore Nat. Lab., Livermore, CA, USA, Tech. Rep. UCRL-51326, 1973.
[61] K. Olejnik, J. Zemek, W.S.M. Werner, Angular-resolved photoelectron spectroscopy of corrugated surfaces, Surf. Sci. 595 (2005) 212–222, https://doi.org/10.1016/j.susc.2005.08.014.
[62] L. Katona, D. Bianchi, J. Brenner, G. Vorlaufer, A. Vernes, G. Betz, W.S.M. Werner, Effect of surface roughness on angle-resolved XPS, Surf. Interface Anal. 44 (2012) 1119–1123, https://doi.org/10.1002/sia.4886.
[63] B.D. Cullity, C.D. Graham, Introduction to magnetic materials, second ed., John Wiley & Sons Inc, Hoboken, 2009.
[64] Z. Yang, S. Wu, Z. Zhao, M.C. Nguyen, S. Yu, T. Wen, L. Tang, F. Li, K.-M. Ho, C.-Z. Wang, Structures and magnetic properties of iron silicide from adaptive genetic algorithm and first-principles calculations, J. Appl. Phys. 124 (2018), 073901, https://doi.org/10.1063/1.5036992.
[65] J.F. Piamba, C. Ortega, R. Hernández-Bravo, J.M. González Carmona, J.A. Tabares, G.A. Pérez Alcázar, J.M. Alvarado-Orozco, Theoretical and experimental study of FeSi on magnetic and phase properties, Appl. Phys. A 126 (2020) 849, https://doi.org/10.1007/s00339-020-04038-8.
[66] S.A. Norris, M.J. Aziz, Ion-Induced Nanopatterning of Silicon: Toward a Predictive Model, Appl. Phys. Rev. 6 (2019), 011311, https://doi.org/10.1063/1.5043438.
[67] R. Cuerno, J.-S. Kim, A Perspective on Nanoscale Pattern Formation at Surfaces by Ion-Beam Irradiation, J. Appl. Phys. 128 (2020), 180902, https://doi.org/10.1063/5.0021308.
[68] E. Anzenberg, C.S. Madi, M.J. Aziz, K.F. Ludwig Jr, Time-resolved measurements of nanoscale surface pattern formation kinetics in two dimensions on ion-irradiated Si, Phys. Rev. B 84 (2011), 214108, https://doi.org/10.1103/PhysRevB.84.214108.
[69] J. Muñoz-García, R. Cuerno, M. Castro, Stress-driven nonlinear dynamics of ion-induced surface nanopatterns, Phys. Rev. B 100 (2019), 205421, https://doi.org/10.1103/PhysRevB.100.205421.
[70] J.C. Perkinson, J.M. Swenson, A. DeMasi, C. Wagenbach, K.F. Ludwig Jr, S. A. Norris, M.J. Aziz, Sawtooth structure formation under nonlinear-regime ion bombardment, J. Phys.: Condens. Matter 30 (2018), 294004, https://doi.org/10.1088/1361-648X/aac460.